Transient neocortical gamma oscillations induced by neuronal response modulation

Farshad Shirani[1] (ORCID)

Abstract

In this paper a mean field model of spatio-temporal electroencephalographic activity in the neocortex is used to computationally study the emergence of neocortical gamma oscillations as a result of neuronal response modulation. It is shown using a numerical bifurcation analysis that gamma oscillations emerge robustly in the solutions of the model and transition to beta oscillations through coordinated modulation of the responsiveness of inhibitory and excitatory neuronal populations. The spatio-temporal pattern of the propagation of these oscillations across the neocortex is illustrated by solving the equations of the model using a finite element software package. Thereby, it is shown that the gamma oscillations remain localized to the regions of neuronal modulation. Moreover, it is discussed that the inherent spatial averaging effect of commonly used electrocortical measurement techniques can significantly alter the amplitude and pattern of fast oscillations in neocortical recordings, and hence can potentially affect physiological interpretations of these recordings.

1 Introduction

Oscillatory patterns of electrical activity in the neocortex, usually measured on the scalp by electroencephalography (EEG) and magnetoencephalography (MEG), or measured intracranially by electrocorticography (ECoG), correlate with numerous states of the operation of the brain. These oscillations can emerge as sustained rhythms, or as transient bursts of fluctuations which last only for few cycles. They are presumed to play a fundamental role in cognition and overall functioning of the brain, possibly by facilitating efficient coordination of neuronal activity across the neocortex. Distinct distortions or disruption of these oscillations can hence be used as a marker for specific diseases. Despite their substantial importance, however, the underlying physiological mechanism of the generation of these cortical oscillations is not yet well-understood (Buzsáki and Watson 2012; Jones 2016; van Ede et al. 2018; Jia and Kohn 2011).

✉ Farshad Shirani
farshad.shirani@georgetown.edu

[1] Department of Mathematics and Statistics, Georgetown University, Washington, DC 20057, USA

Gamma oscillations in the frequency range of 30 to 80 Hz are ubiquitous short-lasting oscillations which usually arise locally in the neocortex and correlate with the operational mode of the underlying cortical network, providing a signature of the engagement of the network. It is hypothesized that gamma oscillations may have a syntactic function in the coordination of information flow across the neocortex. Impaired or irregular gamma oscillations have been observed in psychiatric diseases such as schizophrenia, attention-deficit hyperactivity disorder (ADHD), bipolar disorder, and autism spectrum disorder (ASD), as well as in neurodegenerative diseases such as Alzheimer's disease (AD) and Parkinson's disease (PD), and in neurological disorders such as epilepsy (Buzsáki and Watson 2012; Jia and Kohn 2011; Buzsáki and Wang 2012; Lee and Jones 2013; Knoblich et al. 2010; Kopell et al. 2000; Traub et al. 1999; Cardin et al. 2009; Ray and Maunsell 2015). Therefore, understanding the mechanism of the generation of gamma oscillations can provide important information about the healthy operation of the brain.

Dynamic modulation of the responsiveness of neuronal populations is a fundamental property of cortical networks, which is thought to mediate information flow in the neocortex by rapidly altering the cortical excitability and sensitivity. This dynamic control of the engagement of cortical networks can transiently link local populations of neurons

together over intervals of time ranging from milliseconds to seconds. It is hence hypothesized that this adaptable control of neuronal activity is a basis of diverse perceptual behaviors in the brain (Haider and McCormick 2009). The responsiveness of neurons can be modulated in several ways, through changes in ionic concentrations as well as variations in postsynaptic parameters such as the membrane conductance, the mean membrane potential, and the variance of membrane potential. These modifications can be made through the ongoing barrages of the synaptic inputs that neurons receive from their surrounding network when the network is involved in a sensory-driven activity (Haider and McCormick 2009; Cardin et al. 2008). In addition, neuromodulators can also alter the responsiveness of neurons (McCormick et al. 1993; McCormick 1992). For example, serotonin and catecholamines such as dopamine and noradrenaline are known to modulate the gain of neurons in the prefrontal cortex (Thurley et al. 2008). Furthermore, acetylcholine can multiplicatively modulate neuronal sensitivity in macaque area V1 neurons by acting on muscarinic and nicotinic receptors (Herrero et al. 2017).

In this paper, the biophysical mean field model of electroencephalographic activity proposed by Liley et al. (2002) is used to demonstrate the emergence and propagation of gamma oscillations in the neocortex as a result of neuronal response modulation. This model has been widely used in the literature to study brain rhythms (Bojak et al. 2004; Bojak and Liley 2007), general anesthesia (Wilson et al. 2006a; Liley and Walsh 2013; Bojak et al. 2013; Foster et al. 2008; Bojak et al. 2015; Steyn-Ross et al. 2004), epileptic seizures (Martinet et al. 2017; Kramer et al. 2012; Kramer et al. 2006; Liley and Bojak 2005; Kramer et al. 2005), and sleep (Lopour et al. 2011; Wilson et al. 2006b;

SteynRoss et al. 2005). Tools for numerical implementation of the model and computation of its equilibria and time-periodic solutions are developed by Green and van Veen (2014). Complexity of the dynamic behavior of the model, including the existence of periodic and pseudo-periodic solutions, chaotic behavior, multistability, and dynamic bifurcations are widely studied (Frascoli et al. 2008, 2011; van Veen and Green 2014; van Veen and Lily 2006; Dafilis et al. 2001, 2013, 2015). Rigorous analytical results on well-posedness, regularity, biophysical plausibility, and global dynamics of this model are established by Shirani et al. (2017). Specifically, it is shown that this model can have a noncompact global attracting set and can present a rich variety of spatially localized dynamic behavior.

This paper is organized as follows. In Section 2, the mathematical structure of the model is presented and its variables and parameters are described. In Section 3, it is shown through a codimension-one bifurcation analysis that gamma oscillations emerge robustly in the solutions of the model when neuronal responsiveness is effectively altered. In Section 4, the bifurcation analysis is extended to codimension-two to demonstrate how the emerged gamma oscillations can transition back to resting-state beta oscillations through coordinated modulation of both inhibitory and excitatory neuronal populations. In Section 5, the equations of the model are solved using a finite-element solver and the emergence, spatial propagation, and transition of gamma oscillations are illustrated. Moreover, potential effects of the size and location of electrocortical measurement electrodes on the amplitude and temporal pattern of gamma oscillation recordings are discussed. Finally, the contribution of the results to the understanding of transient gamma oscillations in neocortical activity in the brain are discussed in Section 6.

$$(\tau_E \partial_t + 1)v_E(x,t) = \frac{V_{EE} - v_E(x,t)}{|V_{EE}|}i_{EE}(x,t) + \frac{V_{IE} - v_E(x,t)}{|V_{IE}|}i_{IE}(x,t),$$

$$(\tau_I \partial_t + 1)v_I(x,t) = \frac{V_{EI} - v_I(x,t)}{|V_{EI}|}i_{EI}(x,t) + \frac{V_{II} - v_I(x,t)}{|V_{II}|}i_{II}(x,t),$$

$$(\partial_t + \gamma_{EE})^2 i_{EE}(x,t) = e\Upsilon_{EE}\gamma_{EE}\left[N_{EE}f_E(v_E(x,t)) + w_{EE}(x,t) + g_{EE}(x,t)\right],$$

$$(\partial_t + \gamma_{EI})^2 i_{EI}(x,t) = e\Upsilon_{EI}\gamma_{EI}\left[N_{EI}f_E(v_E(x,t)) + w_{EI}(x,t) + g_{EI}(x,t)\right],$$

$$(\partial_t + \gamma_{IE})^2 i_{IE}(x,t) = e\Upsilon_{IE}\gamma_{IE}\left[N_{IE}f_I(v_I(x,t)) + g_{IE}(x,t)\right],$$

$$(\partial_t + \gamma_{II})^2 i_{II}(x,t) = e\Upsilon_{II}\gamma_{II}\left[N_{II}f_I(v_I(x,t)) + g_{II}(x,t)\right],$$

$$\left[(\partial_t + \nu\Lambda_{EE})^2 - \frac{3}{2}\nu^2\Delta\right]w_{EE}(x,t) = \nu^2\Lambda_{EE}^2 M_{EE}f_E(v_E(x,t)),$$

$$\left[(\partial_t + \nu\Lambda_{EI})^2 - \frac{3}{2}\nu^2\Delta\right]w_{EI}(x,t) = \nu^2\Lambda_{EI}^2 M_{EI}f_E(v_E(x,t)), \qquad (x,t) \in \Omega \times (0,T], \qquad (1)$$

2 Model description

Local networks of cortical neurons are densely interconnected. It is shown, for example, that local networks of inhibitory interneurons within layers II and III in mouse frontal cortex almost form a completely connected graph without any distinct subnetworks (Fino and Yuste 2011; Lee and Huguenard 2011). Such a locally dense structure of the neocortex suggests mean field models as particularly useful models for studying the mesoscopic activity of neocortical neurons being monitored by EEG recordings. The biophysical mean field model developed by Liley et al. (2002) effectively connects the intracortical and corticocortical neuronal activity to EEG measurements from the scalp. For ease of reference, the mathematical structure and description of variables and parameters of this model are given below. Further details of the model are available in the literature (Liley et al. 2002; Bojak and Liley 2005; Shirani et al. 2017; Bojak et al. 2015; Liley and Walsh 2013).

Let $\Omega \subset \mathbb{R}^2$ be an open rectangle defining the domain of the neocortex, so that each point $x = (x_1, x_2) \in \Omega$ indicates the location of a local cortical population. Let E and I denote populations of excitatory and inhibitory neurons, respectively. Then, the system of partial differential equations (PDEs) given by (1), with periodic boundary conditions, provides a mean field model of electroencephalographic activity in the neocortex, wherein ∂_t denotes the partial derivative with respect to t, and Δ

denotes the Laplace operator. For X, Y $\in$ {E, I}, the variable $v_X(x, t)$ in (1) denotes the spatially mean soma membrane potential of a population of type X located at x. Moreover, $i_{XY}(x, t)$ denotes the spatially mean postsynaptic activation of the synapses of a population of type X located at x, onto a population of type Y located at the same point. In addition, $w_{EX}(x, t)$ denotes the mean rate of corticocortical input pulses that a population of type X located at x receives from all other excitatory populations throughout the neocortex. Finally, $g_{XY}(x, t)$ denotes the mean rate of subcortical input pulses of type X received by a population of type Y located at x. Note that v_X and i_{XY} are measured in mV, whereas w_{EX} and g_{XY} are measured in s^{-1}. Moreover, i_{XY}, w_{EX}, and g_{XY} are nonnegative quantities by definition. The constant e in (1) is Napier's constant, and the nonlinear function $f_X(\cdot)$ gives the mean firing rate of a population of type X as a sigmoid function of the population's mean membrane potential, defined as

$$f_X(v_X) := \frac{F_X}{1 + \exp\left(-\sqrt{2}\,\dfrac{v_X - \mu_X}{\sigma_X}\right)}, \quad X \in \{E, I\}. \quad (2)$$

Definition of the biophysical parameters of the model and their range of values are given in Table 1. As in Shirani et al. (2017), in addition to the notational changes to the original equations given by Liley et al. (2002), the reference of electric potentials of each population is set at the resting

Table 1 Biophysical parameters of the mean field model (1). All electric potentials are given with respect to the mean resting soma membrane potential $v_{rest} = -70$ mV, Bojak and Liley (2005) and Shirani et al. (2017)

Parameter	Definition	Range	Unit
τ_E	Passive excitatory membrane decay time constant	[0.005, 0.15]	s
τ_I	Passive inhibitory membrane decay time constant	[0.005, 0.15]	s
V_{EE}, V_{EI}	Mean excitatory Nernst potentials	[50, 80]	mV
V_{IE}, V_{II}	Mean inhibitory Nernst potentials	[−20, −5]	mV
γ_{EE}, γ_{EI}	Excitatory postsynaptic potential rate constants	[100, 1000]	s^{-1}
γ_{IE}, γ_{II}	Inhibitory postsynaptic potential rate constants	[10, 500]	s^{-1}
$\Upsilon_{EE}, \Upsilon_{EI}$	Amplitude of excitatory postsynaptic potentials	[0.1, 2.0]	mV
$\Upsilon_{IE}, \Upsilon_{II}$	Amplitude of inhibitory postsynaptic potentials	[0.1, 2.0]	mV
N_{EE}, N_{EI}	Number of intracortical excitatory connections	[2000, 5000]	—
N_{IE}, N_{II}	Number of intracortical inhibitory connections	[100, 1000]	—
ν	Corticocortical conduction velocity	[100, 1000]	cm/s
$\Lambda_{EE}, \Lambda_{EI}$	Decay scale of corticocortical excitatory connectivities	[0.1, 1.0]	cm^{-1}
M_{EE}, M_{EI}	Number of corticocortical excitatory connections	[2000, 5000]	—
F_E	Maximum mean excitatory firing rate	[50, 500]	s^{-1}
F_I	Maximum mean inhibitory firing rate	[50, 500]	s^{-1}
μ_E	Excitatory firing threshold potential	[15, 30]	mV
μ_I	Inhibitory firing threshold potential	[15, 30]	mV
σ_E	Standard deviation of excitatory firing threshold potential	[2, 7]	mV
σ_I	Standard deviation of inhibitory firing threshold potential	[2, 7]	mV

potential of the population in order to avoid the constant terms that would otherwise appear in (1).

The first two equations in (1) represent the first-order dynamics of the resistive-capacitive membrane of space-averaged neurons; see the details in Liley et al. (2002) and Shirani et al. (2017). The next four critically damped second-order equations generate postsynaptic α-functions in response to impulse inputs. The last two telegraph equations in (1) model the propagation of excitatory axonal pulses along long-range corticocortical fibers. The key variable in this model is the mean membrane potential of excitatory populations v_E. It is presumed in the literature that v_E is linearly proportional to EEG recordings from the scalp (Liley et al. 2002; Liley and Walsh 2013). Therefore, the spatio-temporal pattern of variations of v_E is illustrated throughout this paper as the predictions provided by the model for EEG measurements.

3 Neuronal response modulation and emergence of gamma oscillations

The input-output relationships that characterize neuronal responsiveness in cortical networks usually follow sigmoid curves, that is, changes in intermediate values of the input result in large variations in the neuronal response, whereas changes in the input values below a threshold level or above a saturation level do not evoke substantial variations in the response (Haider and McCormick 2009; Thurley et al. 2008). Such characteristic response curves can be modulated in different ways, resulting in different neuronal behaviors. The *sensitivity* of a neuron is equally altered at all input levels if its response curve is stretched or shrunk along the output axis by a multiplicative factor (Cardin et al. 2008; Ni et al. 2016; Haider and McCormick 2009). This neuronal gain modulation changes the slope and

maximum level of the curve while leaving the threshold and saturation levels unchanged. Shifting the curve right or left along the input axis alters the *excitability* of a neuron, that is, its responsiveness to different levels of the input. Although the shape of the curve remains unchanged in this case, an input gain modulation is attained by shifts in the threshold and saturation levels (Cardin et al. 2008; Haider and McCormick 2009). Finally, the *saliency* of a neuron can be altered by stretching or shrinking its response curve along the input axis, which changes the maximum slope of the curve and moves the threshold and saturation levels in opposite directions (Herrero et al. 2017). A combination of these modulatory effects can also result from the action of neuromodulators. For example, it is shown by Thurley et al. (2008) that, mediated by D1 receptors, dopamine can increase the excitability of Layer V pyramidal neurons in rat prefrontal cortex by shifting the firing rate-current response curve of neurons to lower inputs. In addition, it increases the maximum slope (saliency) of the curve at intermediate values of current and decreases the maximum level of the firing rate response.

As shown in Fig. 1, the different types of neuronal gain modulation described above can be effectively incorporated into the model (1) using the graph of the sigmoid firing rate functions (2) as the characteristic curves of neuronal responsiveness. In this section, the characteristic curve of inhibitory populations is used to predict the emergence of gamma oscillations in the solutions of (1) when the parameters of the curve are changed effectively. Inhibitory neuronal activity in cortical networks is integral to network oscillations and rapid coordination of functional connectivity across the cortex, (Cardin et al. 2009; Whittington et al. 2000; Haider and McCormick 2009; Buzsáki and Watson 2012; Buzsáki and Wang 2012; Ray and Maunsell 2015; Knoblich et al. 2010; Jia and Kohn 2011). Moreover, neuronal modulations such
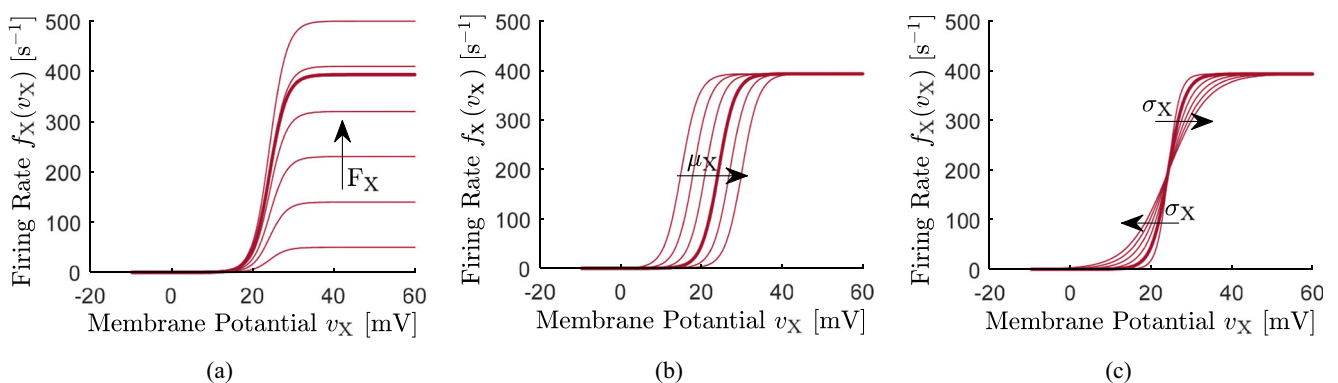

Fig. 1 Neuronal gain modulation. Thick curves show the firing rate function (2) for $X = I$ and the nominal parameter values given in Table 2. Other curves in each graph illustrate variations in the shape of nominal curves as F_X, μ_X and σ_X, $X \in \{E, I\}$, change over their range of values given in Table 1. Arrows indicate variations corresponding to incremental changes in parameter values

as modulation through nicotinic and muscarinic receptors occur predominately on inhibitory interneurons (Herrero et al. 2017).

In this section, predictions on the emergence of gamma oscillations are based on codimension-one bifurcation analysis of a spatially homogeneous version of (1), that is, the model with spatially homogeneous initial values and subcortical inputs. Moreover, to effectively analyze the internal dynamics of the model, the subcortical inputs are assumed to be constant in time. This approximate model is a system of ordinary differential equations (ODEs) obtained from (1) by omitting the Laplacian terms $-\frac{3}{2}\nu^2\Delta$. Bifurcations of equilibria and limit cycles of this system of ODEs can be effectively analyzed using available numerical continuation and bifurcation analysis tools. Moreover, the dynamic behavior of this approximate model can be interpreted as the dynamic behavior of a local cortical network, since omitting the Laplacian terms in the equations is equivalent to considering the corticocortical conduction velocity of zero. Therefore, the possibility of the original model (1) having highly localized dynamic activity, as shown by Shirani et al. (2017), implies that the predictions made by analyzing this approximate model can result in meaningful predictions on the emergence of gamma oscillations in the solutions of the original model. This is demonstrated in Section 5, where the solutions of the full system of PDEs given by (1) are computed using a finite-element solver package.

In this section, as well as in Section 4, the numerical analysis of the ODE system is performed using MatCont (Dhooge et al. 2008) for the nominal parameters values given in Table 2. Note that inhibitory inputs from subcortical regions are rare. Therefore, g_{IE} and g_{II} are set equal to zero. The excitatory subcortical inputs g_{EE} and g_{EI} are set to be constant and, respectively, equal to $\bar{g}_{EE}$ and $\bar{g}_{EI}$ given in Table 2. For this set of inputs and parameter values, the

ODE system possesses a single stable equilibrium in the biophysically reasonable region of its phase space.

3.1 Neuronal sensitivity modulation

As shown in Fig. 1a, changes in F_I results in multiplicative changes of neuronal sensitivity in inhibitory populations. To observe the effect of this response modulation on the dynamic behavior of the spatially homogeneous system, the equilibrium of the ODE system is continued in both forward and backward directions when F_I is free to change over its range of values given in Table 1. The resulting curve of equilibria is shown in Fig. 2a. The system undergoes two Hopf bifurcations, denoted by H_1 and H_2, and two fold bifurcations, denoted by F_1 and F_2. The limit cycles originating from Hopf bifurcation points are also continued and the curves of minimum and maximum values taken by ν_E on the resulting cycles are shown in Fig. 2a. The frequency of oscillations on these cycles are shown in Fig. 3a. It is observed that, as F_I decreases below the value associated with the Hopf bifurcation point H_1, the stable equilibrium becomes unstable. Moreover, the limit cycles originating from H_1 are unstable, whereas those originating from H_2 are stable. At extremely large values of F_I, the curves of stable and unstable limit cycles collide tangentially at a fold bifurcation of limit cycles. This bifurcation is not made visible in Fig. 2a, since it occurs at biophysically implausible values of F_I.

The Hopf bifurcation H_1 described above is of particular interest. The frequency of unstable cycles originating from this bifurcation point lies between 13 and 15 Hz, suggesting that the damped oscillations around the stable equilibrium at nominal parameter values are in the resting-state low beta (alpha) frequency band. More importantly, as the stable equilibrium switches to an unstable equilibrium at this bifurcation point, orbits of the system depart the vicinity

Table 2 The set of biophysically plausible parameter values used as the nominal values for the computational analysis of Sections 3–5 (Bojak and Liley 2005, Table V, col. 11). The parameters $\bar{g}_{EE}$, $\bar{g}_{EI}$, $\bar{g}_{IE}$, and $\bar{g}_{II}$ are the mean values of the physiologically shaped random inputs g_{EE}, g_{EI}, g_{IE}, and g_{II} used by Bojak and Liley (2005), respectively. Electric potentials are given with respect to the mean resting membrane potentials $v_{E_{rest}} = -72.293$ mV and $v_{I_{rest}} = -67.261$ mV

| Parameter	τ_E	τ_I	V_{EE}	V_{EI}	V_{IE}	V_{II}	γ_{EE}
Value	32.209×10^{-3}	92.260×10^{-3}	79.5513	77.0967	-8.404	-9.413	122.68
Parameter	γ_{EI}	γ_{IE}	γ_{II}	Υ_{EE}	Υ_{EI}	Υ_{IE}	Υ_{II}
Value	982.51	293.10	111.40	0.29835	1.1465	1.2615	0.20143
Parameter	N_{EE}	N_{EI}	N_{IE}	N_{II}	ν	$\Lambda_{EE}, \Lambda_{EI}$	M_{EE}
Value	4204.4	3602.9	443.71	386.43	116.12	0.60890	3228.0
Parameter	M_{EI}	F_E	F_I	μ_E	μ_I	σ_E	σ_I
Value	2956.9	66.433	393.29	27.771	24.175	4.7068	2.9644
Parameter	$\bar{g}_{EE}$	$\bar{g}_{EI}$	$\bar{g}_{IE}$	$\bar{g}_{II}$			
Value	2250.6	4363.4	0	0			
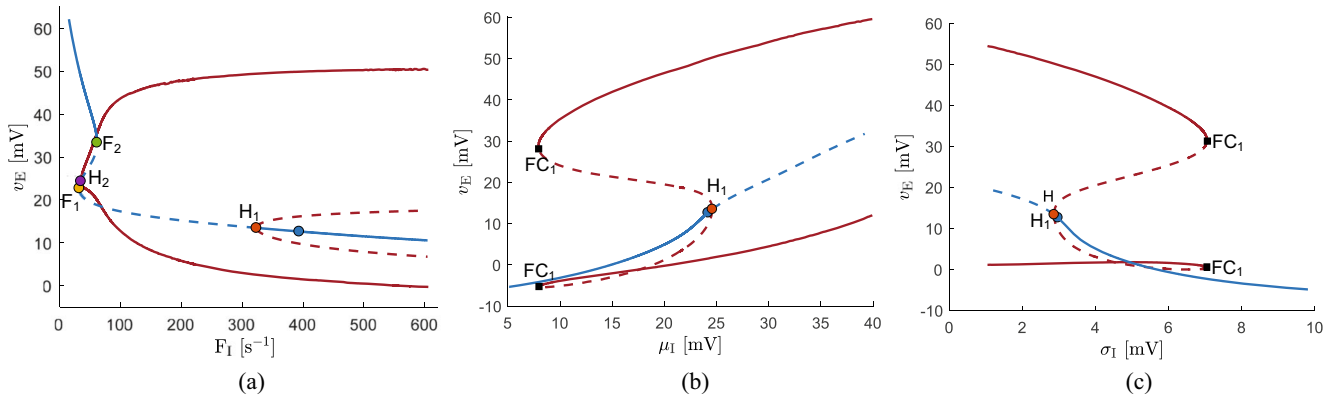
Fig. 2 Codimension-one bifurcation diagrams of the ODE system described in Section 3. Curves of equilibria are shown in blue. Curves of the minimum and maximum values that v_E takes on the limit cycles are shown in red. The reference of electric potential for v_E is the mean resting soma membrane potential $v_{E_{rest}} = -72.293$ mV. Solid lines indicate stable equilibria and limit cycles. Dashed lines indicate unstable equilibria and limit cycles. Blue dots show the stable equilibrium of the system for the nominal parameter values given in Table 2. Fold and Hopf bifurcation points are indicated by F and H, respectively. Fold bifurcations of limit cycles are indicated by FC. The Hopf bifurcation points and the fold bifurcation of limit cycles that occur at biophysically implausible parameter values are not made visible. **a** the bifurcation diagram for F_I as a free parameter, **b** the bifurcation diagram for μ_I as a free parameter, and **c** the bifurcation diagram for σ_I as a free parameter

of the equilibrium and converge to a stable limit cycle originated from the Hopf bifurcation H_2. As shown in Fig. 3a, stable oscillations on this cycle lie in the gamma frequency band. This predicts that gamma oscillations can emerge in cortical networks when the sensitivity of inhibitory neuronal populations is reduced by modulatory actions.

3.2 Neuronal excitability modulation

Figure 1b shows that changes in μ_I shifts the characteristic curve of inhibitory neuronal populations along the horizontal axis, thereby changing their excitability in response to variations in the mean membrane potential. Continuation of the equilibrium of the ODE system for the free parameter μ_I gives the curve of equilibria shown in Fig. 2b. When μ_I increases from its nominal value, the system undergoes

a Hopf bifurcation of equilibrium denoted by H_1. The stability of the equilibrium switches at this bifurcation point. Continuation of the limit cycles origination from H_1 reveals a fold bifurcation of limit cycles at low values of μ_I, which is denoted by FC_1. This further reveals the existence of a curve of stable limit cycles. Therefore, when μ_I increases above the bifurcation value, orbits of the system departing the vicinity of the unstable equilibrium converge to a stable limit cycle. As shown in Fig. 3b, the frequency of oscillations on stable cycles lies in the gamma band, and hence this predicts the emergence of gamma oscillations in the electrocortical activity when the neuromodulation decreases the excitability of inhibitory populations by shifting their response curve to higher input values. It should be noted that if μ_I is free to increase to biophysically implausible values, a second Hopf bifurcation H_2 is detected on the curve of equilibria where the unstable equilibrium switches to a
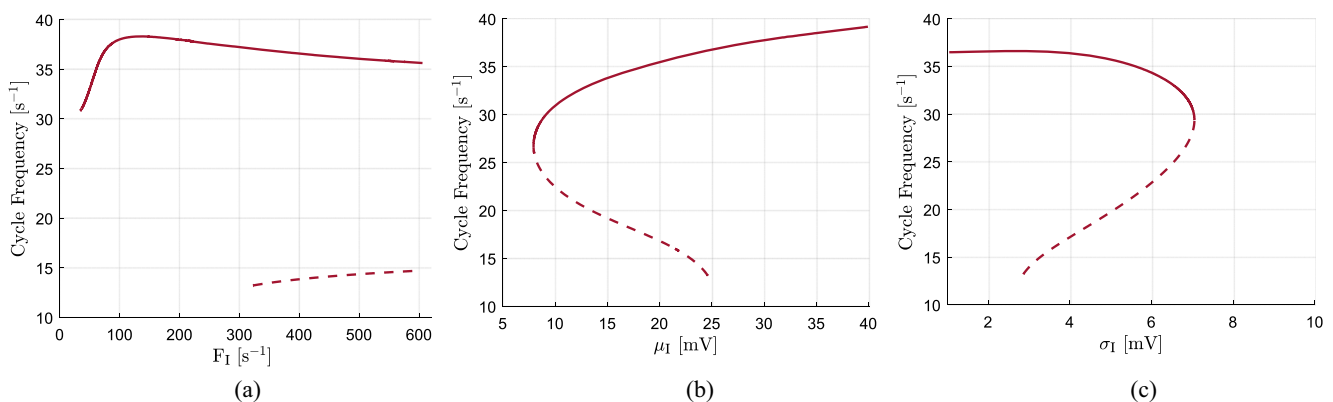

Fig. 3 Frequency of the limit cycles in the bifurcation diagrams shown in Fig. 2

stable equilibrium. A second fold bifurcation of limit cycles FC_2 is also detected on the curve of limit cycles. These bifurcations are not made visible in Fig. 2b as they appear at extremely large values of μ_I.

3.3 Neuronal saliency modulation

The maximum slope of response curves can be altered by changing σ_I, as shown in Fig. 1c. The bifurcation diagram shown in Fig. 2c implies that a Hopf bifurcation at lower values of σ_I makes the equilibrium unstable. Continuation of the unstable limit cycles originating from this bifurcation point reveals the existence of a stable limit cycle and a fold bifurcation of limit cycles. The orbits of the system converge to a stable limit cycle when σ_I decreases below the Hopf bifurcation value. Figure 3c shows that the oscillations on this stable cycle are in the gamma frequency band. Therefore, it is predicted by these results that enhancement of the saliency of inhibitory neuronal networks can induce gamma oscillations in the network. Note that at implausibly small values of σ_I the system undergoes a second Hopf bifurcation and a fold bifurcation of limit cycles, which are not made visible in Fig. 2c.

4 Transition to beta oscillations

Oscillatory patterns of electrocortical activity in the neuronal networks that are involved in cognitive functions, such as gamma oscillations, are usually transient phenomena which emerge briefly in the underlying network and disappear once the cognitive task is processed and the initial state of the network is restored (Buzsáki and Watson 2012; Jones 2016; Traub et al. 1999). However, the bifurcation analysis performed in Section 3 does not explain a biophysically reasonable mechanism for transition from the emerged gamma oscillations back to the resting-state low beta oscillations. This can be seen through the bifurcation diagrams shown in Fig. 2.

Once F_I decreases below the value corresponding to the first Hopf bifurcation in Fig. 2a, orbits of the system converge to a stable limit cycle and oscillate at gamma frequency. However, increasing F_I back to its nominal value cannot force the orbits to depart a stable cycle and converge back to the equilibrium. Additional increments of F_I only shift the orbits to another stable cycle of larger v_E-amplitude along the curve of limit cycles. Although this predicts significant robustness for the emergence of gamma oscillations, it cannot explain their transitions back to the initial state. As stated in Section 3.1, further continuation of the limit cycles for larger values of F_I identifies a value at which a fold bifurcation of limit cycles occurs as the curves of stable and unstable limit cycles collide.

Therefore, if F_I increases beyond this bifurcation value, the sustained oscillations are terminated and orbits converge to a stable equilibrium. This further allows restoring the initial state through a hysteresis loop. However, the fold bifurcation value of F_I involved in this loop is too large to be biophysically plausible. Alternatively, the bifurcation diagram shown in Fig. 2a also predicts the possibility of the termination of gamma oscillations at very small values of F_I, below the value corresponding to the Hopf bifurcation point H_2. At this range of values of F_I, however, the dynamics of the system is extremely sensitive to small variations in F_I so that the orbits of the system can easily converge to equilibrium values which are not biologically realistic.

When gamma oscillations arise through the modulation of μ_I, the initial resting-state can be restored through a hysteresis loop. This is shown in Fig. 4a. Stable oscillations on limit cycles are terminated when μ_I decreases below the value corresponding to the fold bifurcation of limit cycles FC_1. Orbits of the system converge to a stable equilibrium which moves along the curve of equilibria as μ_I increases back to its nominal value. Similar to the hysteresis loop
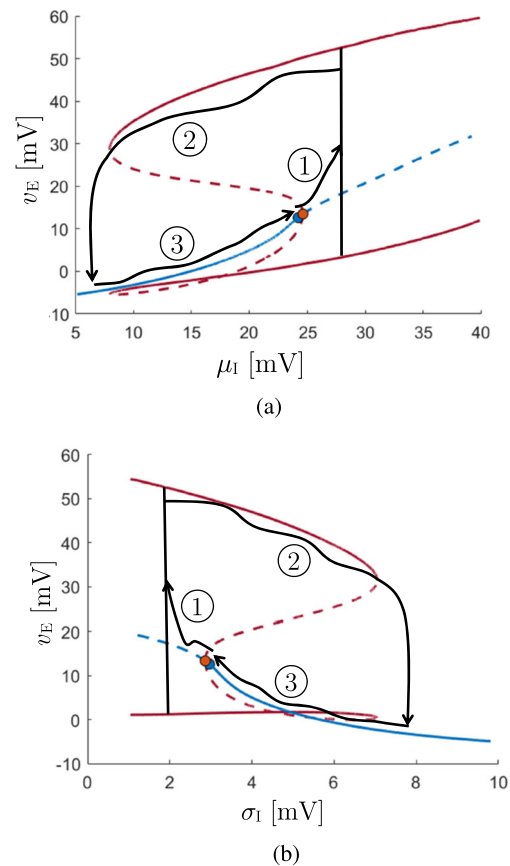

(a)

(b)

Fig. 4 Restoration of the initial state by modulation of the inhibitory parameters through large hysteresis loops. Step 1: induction of gamma oscillations, Step 2: termination of the gamma oscillations, and Step 3: restoration of the initial parameter value. **a** modulatory actions on μ_I and **b** modulatory actions on σ_I

described above for modulation of F_I, this mechanism of transition to initial beta oscillations may not be realistic as it involves very small values of μ_I, corresponding to extreme enhancement of neuronal excitability. Similarly, Fig. 4b implies the possibility of restoring the initial state through a hysteresis loop that involves drastic modulation of σ_I that substantially diminishes the neuronal saliency.

The mechanisms of the emergence of gamma oscillations described in Section 3 and discussed above are based only on the modulation of inhibitory neuronal populations. However, gamma oscillations typically arise from coordinated interaction of inhibitory and excitatory networks (Buzsáki and Wang 2012; Haider and McCormick 2009). In general, cortical networks remarkably maintain a balance of excitation and inhibition during their operation, so that increases in the level of excitation in a cortical region is often accompanied by increases in the level of inhibition. Since long-range corticocortical connections are predominantly excitatory, such an effective balancing of excitation and inhibition must be controlled locally (Haider and McCormick 2009; Dehghani et al. 2016). Due to this locality, the approximate ODE system used in Section 3 can also be helpful in predicting the results of coordinated modulation of both inhibitory and excitatory populations. In what follows, the codimension-one bifurcation analysis of Section 3 is extended to codimension two by additionally considering the parameters of excitatory populations as

free parameters. The analysis provides a biologically reasonable explanation for restoration of the initial state after the emergence of gamma oscillations.

Two-parameter continuation of the codimension-one bifurcation points shown in Fig. 2 results in the bifurcation curves shown in Fig. 5. Specifically, continuation of the adjacent fold and Hopf bifurcation points F_1 and H_2 shown in Fig. 2a reveals a fold-Hopf (or zero-Hopf) codimension-two bifurcation at low values of F_E and F_I, where the resulting curves of fold and Hopf bifurcations intersect each other. This is shown in Fig. 5a. No codimension-two bifurcations are detected along the curve of bifurcations as μ_E and μ_I change over their biophysically reasonable range of values. Similarly, continuation of the bifurcation points as σ_E and σ_I change over their biophysically plausible range of values does not detect any codimension-two bifurcations.

The absence of codimension-two bifurcations along nearly the entire extent of the bifurcation curves in Fig. 5 implies that the overall picture of the codimension-one bifurcation diagrams shown in Fig. 2 remains the same when the characteristic parameters of the excitatory populations are allowed to change freely. Moreover, the moderate slope of the bifurcation curves suggest a fair level of robustness for predictions made based on these diagrams. Therefore, to illustrate a global picture of the dynamics of the ODE system when both excitatory and inhibitory characteristic parameters are free to change, a number of

Fig. 5 Two-parameter continuation of the bifurcation points shown in Fig. 2. The starting bifurcation points are indicated by dots with the same colors as they appear in Fig. 2. The curves shown in gray are the result of the continuation of the fold bifurcation of limit cycles that are not made visible in Fig. 2. **a** continuation for F_I and F_E as free parameters. The detected codimension-two zero-Hopf bifurcation point is indicated by ZH. **b** continuation for μ_I and μ_E as free parameters. The curve shown in purple is the result of the continuation of the Hopf bifurcation point H_2 that is not made visible in Fig. 2b. **c** continuation for σ_I and σ_E as free parameters
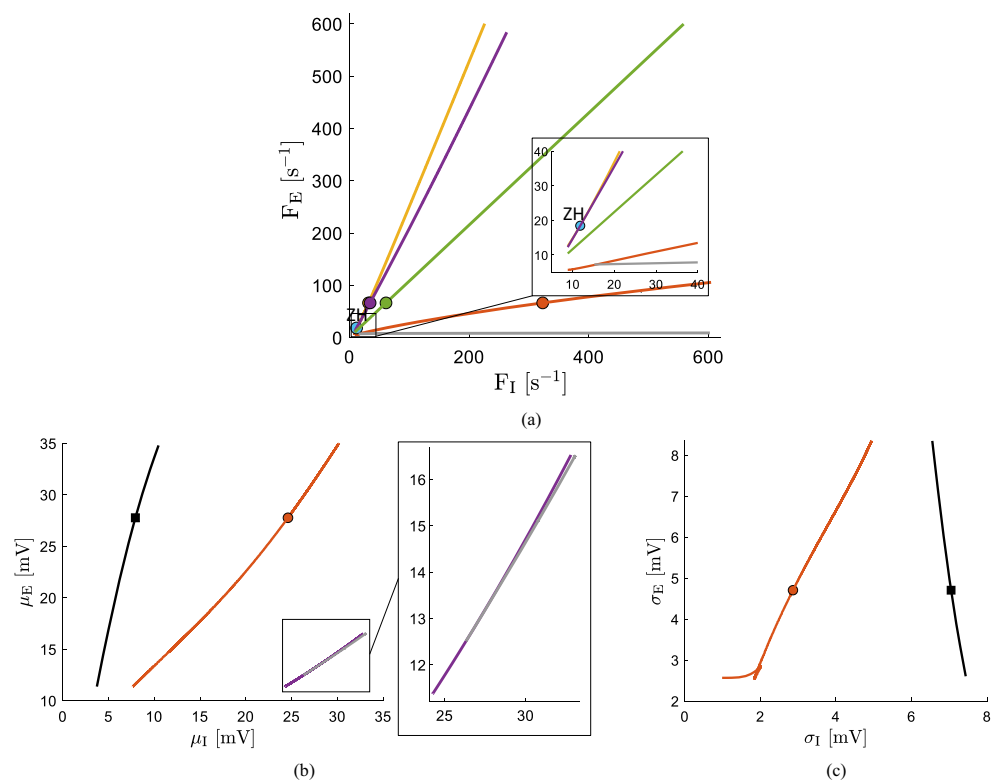
points are picked from the curves of Hopf bifurcations in Fig. 5 and the equilibria and limit cycles originated from these points are continued with respect to inhibitory parameters. The resulting sequence of bifurcation diagrams are shown in Fig. 6, and the frequency of oscillations on the limit cycles are shown in Fig. 7. It is observed that the frequency of stable cycles lies predominantly in the gamma band for almost entire range of parameter values of the characteristic curves, which further implies the robustness of emergent gamma oscillations to perturbations in parameters.

Although the bifurcation diagrams within each sequence of diagrams shown in Fig. 6 generally resemble each other, the location of the bifurcation points and, in particular, the fold bifurcations of limit cycles changes significantly when the parameters of excitatory populations change. As shown in Fig. 6a, the fold bifurcation of limit cycles, which occurs at nonphysiologically large values of F_I when F_E takes its nominal value, moves to lower and biophysically plausible

values when F_E is decreased. As a result, the curves of limit cycles shrink significantly in size. Similarly, it is implied from the sequence of diagrams shown in Fig. 6b that the second Hopf bifurcation of equilibria H_2 and the second fold bifurcation of limit cycles FC_2, which occur at extremely large values of μ_I when μ_E takes its nominal value, move to biophysically plausible values when μ_E is decreased. Finally, Fig. 6c shows that the fold bifurcation of limit cycles FC_1 which occurs at the nominal value of σ_E moves to biophysically more reasonable values of σ_I when σ_E is increased.

The specific changes within each sequence of bifurcation diagrams shown in Fig. 6 suggest biologically reasonable mechanisms for transition between gamma and beta oscillations through coordinated modulation of inhibitory and excitatory neuronal responsiveness. The stepwise parameter modulations shown in Fig. 8 demonstrate these possible mechanisms. As shown in Fig. 8a, in Step 1, decreasing F_I from its nominal value below the value

Fig. 6 Sequences of codimension-one bifurcation diagrams for different values of excitatory parameters. Inhibitory parameters are used as free parameters for generating each diagram. The diagrams shown by thick lines are the same codimension-one diagrams shown in Fig. 2 for the nominal value of excitatory parameters. **a** the sequence of diagrams for different values of F_E when F_I is used as the free parameter. **b** the sequence of diagrams for different values of μ_E when μ_I is used as the free parameter. **c** the sequence of diagrams for different values of σ_E when σ_I is used as the free parameter
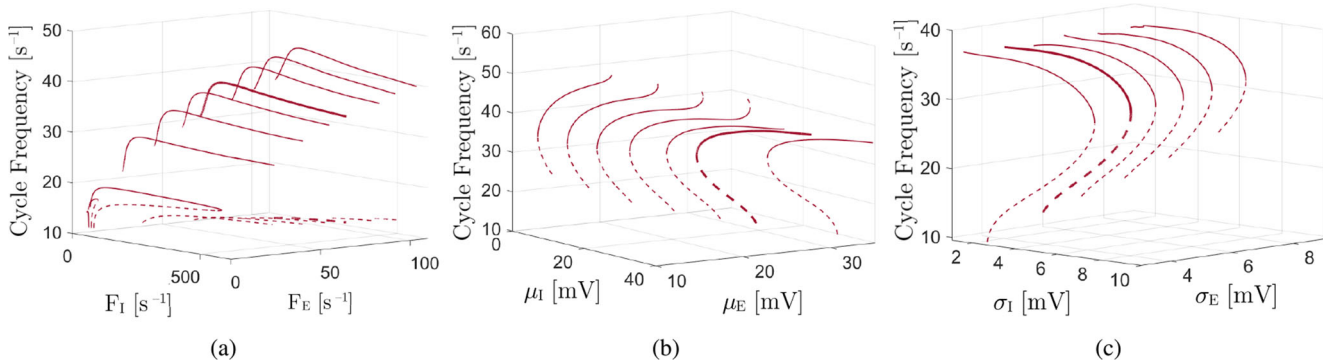

(a)

(b)

(c)
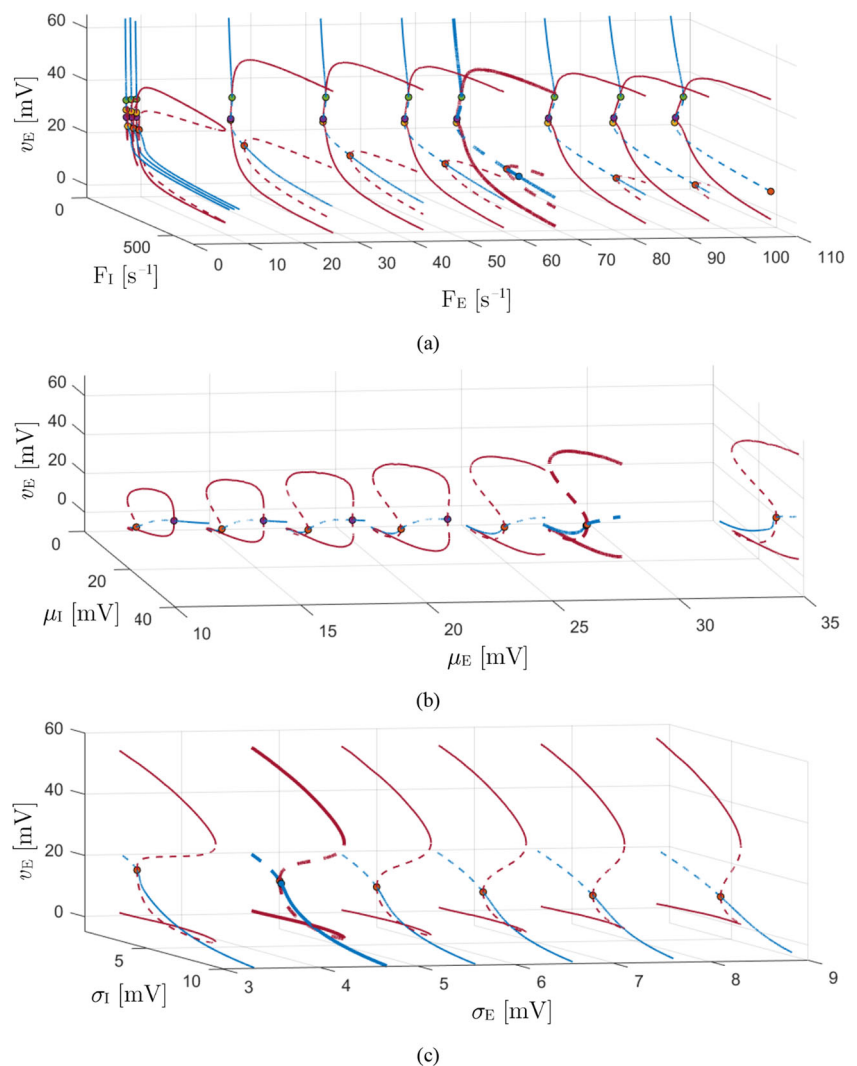
Fig. 7 Frequency of the limit cycles in the sequences of bifurcation diagrams shown in Fig. 6

corresponding to the Hopf bifurcation H_1 results in the emergence of gamma oscillations. This is the same result predicted in Section 3. In Step 2, sufficient reduction in F_E to the level at which the curve of limit cycles shrinks substantially results in termination of gamma oscillations and transition to low beta oscillations. The initial resting-state can then be restored by increasing F_I back to its nominal value in Step 3, followed by increasing F_E to its nominal value in Step 4. This coordinated modulation of neuronal activity is consistent with the essential operational property of cortical networks, that is, maintaining a balance of excitation and inhibition. The decrement in F_E in Step 2 is in the direction to compensate for the imbalance created in the network by the decremental modulation of F_I in Step 1. Similarly, in Step 3, the balanced neuronal activity is perturbed when the modulatory effect on F_I vanishes and F_I increases back to its nominal value. This imbalance is compensated by the increment in F_E in Step 4, so that the initial balanced state is restored. Figure 8b demonstrates a similar mechanism of inducing transient gamma oscillations through coordinated modulation of neuronal excitability (μ_I and μ_E). As shown in Fig. 8c, transition of gamma

oscillations through modulation of neuronal saliency (σ_I and σ_E), however, still requires modulation of σ_I through a hysteresis loop. However, when coordinated with the intermediate excitatory modulation shown in Fig. 8c, the hysteresis loop is reduced in size and becomes biophysically more reasonable.

The mechanisms described above are expressed as stepwise procedures for simplicity of exposition. In fact, there can be overlaps between the steps and the neuronal modulation in each step is not necessitated to begin after completion of modulatory actions in previous steps. However, as implied by the bifurcation diagrams of Figs. 5 and 6, in order for these mechanisms to work properly, it is necessary that the modulation of excitatory populations in Step 2 sufficiently lags the initial modulation of inhibitory populations in Step 1, so that the system undergoes the Hopf bifurcation and gamma oscillations emerge. Otherwise, the system simply exhibits damped oscillations of beta frequency about the stable equilibrium which moves as the neuronal parameters change.

The courses of modulatory actions described above are initiated by the modulation of inhibitory populations
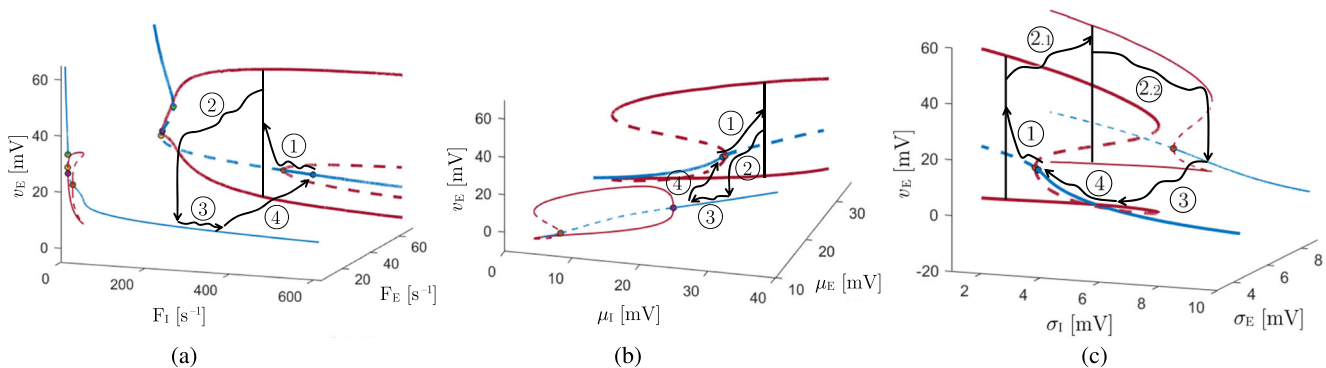

Fig. 8 Mechanisms of transient emergence of gamma oscillations through coordinated modulation of inhibitory and excitatory neuronal responsiveness. Step 1: induction of gamma oscillations by modulation of inhibitory populations. Step 2: termination of the gamma oscillations by modulation of excitatory populations. Steps 3 and 4:

restoration of the initial parameter values. **a** neuronal sensitivity modulation through actions on F_I and F_E. **b** neuronal excitability modulation through actions on μ_I and μ_E. **c** neuronal saliency modulation through actions on σ_I and σ_E. An additional step of modulation of σ_I to larger values is still necessary to terminate the oscillations in Step 2

first, which results in a Hopf bifurcation and gives rise to gamma oscillations. Likewise, the curves of Hopf bifurcations shown in Fig. 5 also predict the emergence of gamma oscillations induced by modulation of excitatory populations. However, the bifurcation diagrams of Fig. 6 imply that, unlike the oscillations induced by inhibitory modulations, transition to beta oscillations in this case cannot analogously result from a subsequent modulation of inhibitory populations that re-establishes the network balance. In fact, modulation of the excitatory parameters in the direction shown in Step 2 in Fig. 8 is necessary for termination of the emerged oscillations, regardless of the type of modulation (inhibitory or excitatory) used initially in the first step to give rise to the gamma oscillations. This can be best understood through the sequence of diagrams shown in Fig. 6a. When F_E increases sufficiently from its nominal value, the system undergoes a Hopf bifurcation and gamma oscillations emerge. However, subsequent modulation of F_I to a biophysically reasonable level, either incremental or decremental, does not terminate the oscillations in a way that allows for restoration of the initial state. In order for this transition to be possible, F_E must be subsequently decreased to the level at which curves of limit cycles shrink substantially in size, so that the oscillations are terminated and orbits converge to a physiological equilibrium. Therefore, when gamma oscillations are induced by modulation of excitatory parameters, restoration of the initial resting-state involves modulatory actions on these parameters through large hysteresis loops.

5 Spatial propagation of gamma oscillations

The numerical analysis of Sections 3 and 4 is based on a spatially homogeneous version of (1), which equivalently represents the dynamics of local cortical networks as a system of ODEs. In this section, the full system of PDEs given by (1) is used to demonstrate the emergence and spatial propagation of gamma oscillations across the neocortex based on the mechanisms predicted in Sections 3 and 4. The computational results are presented only for neuronal sensitivity modulation, that is, the multiplicative modulation of neuronal responsiveness by changing F_I and F_E. This type of response modulation which is often referred to as *neuronal gain modulation*, as well as the neuronal excitability modulation, is widely observed in experimental studies of cortical networks (Cardin et al. 2008; Ni et al. 2016; Haider and McCormick 2009; Disney et al. 2007; Herrero et al. 2017). Although not presented here, the neuronal excitability and saliency modulations described in Sections 3 and 4 yield similar results.

To perform the computations, the domain of the neocortex is set as $\Omega = (0, 60) \times (0, 60)$ mm^2. This is much smaller than the actual human neocortex, but it is sufficiently large for the computational analysis of this section due to the spatial locality of the emergent activity. The time horizon of computations is set as $T = [0, 1100]$ ms. Neuronal gain modulation is assumed to be attained, for example, by diffusion of neuromodulators into two circular regions of radius $R = 15$ mm centered at locations $a = (15, 15)$ and $b = (45, 45)$. These regions are denoted as region A and region B, respectively. In both regions, F_I is decreased from its nominal value to $\tilde{F}_I = 275$ s^{-1} at time $t_{I_1} = 50$ ms, and is increased back to its nominal value at $t_{I_2} = 700$ ms. Note that $\tilde{F}_I$ is below the bifurcation value shown in Fig. 2a, and hence the results of Section 3 predict the emergence of gamma oscillations. To show the necessity of subsequent decrease in F_E for transition to beta oscillations, F_E is decreased only on region A, from its nominal value to $\tilde{F}_E = 7$ s^{-1} at $t_{E_1} = 500$ ms, and is increased back to its nominal value at $t_{E_2} = 1000$ ms. Therefore, the modulatory actions in region A follow the course of modulations shown in Fig. 8a and the initial resting state is expected to be restored in this region.

To include these modulatory actions in the equations of the model, let

$$\eta(t) := \frac{1}{1 + \exp\left(-\dfrac{t}{\rho}\right)},$$

$$\phi(x) := \begin{cases} \exp\left(1 + \dfrac{1}{\left\|\dfrac{x}{R}\right\|^2 - 1}\right), & \text{if } \|x\| < R, \\ 0, & \text{if } \|x\| \geq R, \end{cases}$$

where ρ adjusts the sharpness of transition from 0 to 1 in $\eta(t)$, and $\|\cdot\|$ denotes the Euclidean norm in $\mathbb{R}^2$. Setting $\rho = 5$ ms, the value of $\eta(t)$ smoothly switches from 0 to 1 at $t = 0$ over an approximate transition interval of $6\rho = 30$ ms. The function ϕ takes its maximum value 1 at $x = 0$ and radially decreases to 0 as x approaches the boundary of the disk $\|x\| \leq R$. The neuronal gain modulations described above are then incorporated into (1) by substituting the following two smooth functions for parameters F_I and F_E,

$$F_I(x, t) = \mathring{F}_I + (\tilde{F}_I - \mathring{F}_I)\left[\eta(t - t_{I_1}) - \eta(t - t_{I_2})\right]\phi(x - a)$$
$$+ (\tilde{F}_I - \mathring{F}_I)\left[\eta(t - t_{I_1}) - \eta(t - t_{I_2})\right]\phi(x - b),$$
$$F_E(x, t) = \mathring{F}_E + (\tilde{F}_E - \mathring{F}_E)\left[\eta(t - t_{E_1}) - \eta(t - t_{E_2})\right]\phi(x - a),$$

where $\mathring{F}_I$ and $\mathring{F}_E$ denote the nominal values of F_I and F_E given in Table 2, respectively.

Depending on the specific purpose of numerical computations, subcortical inputs are usually modeled as physiologically shaped random inputs (Bojak and Liley 2005).

However, for clearer illustration of the emergence and propagation pattern of gamma oscillations, and for better comparison of the results with predictions of Sections 3 and 4, in the computations of this section g_{EE}, g_{EI}, g_{IE}, and g_{II} are set to take the same constant values as considered for the approximate ODE system in Sections 3 and 4. Moreover, other than F_I and F_E which are modulated as described above, the rest of the parameters of the model take their nominal values given in Table 2, the same as that considered for the analysis of Sections 3 and 4. For this set of inputs and nominal parameters, the spatially homogeneous stable equilibrium of (1) can be calculated as

$$(v_E^*, v_I^*) = (12.6326, 13.319),$$
$$(i_{EE}^*, i_{EI}^*, i_{IE}^*, i_{II}^*) = (49.0506, 28.3164, 11.4371, 4.1846),$$
$$(w_{EE}^*, w_{EI}^*) = (2245.7, 2057.1).$$

The initial values of the variables are assumed to be constant over Ω. The initial value of v_E is set as $v_{E_0} = 1.2v_E^*$, and the rest of variables are initially set at their equilibrium given above.

The solutions of the model are computed using the finite-element-based software COMSOL Multiphysics® version

5.3a. As stated in Section 2, the boundary condition of the problem is set to be periodic. A triangular mesh is generated with maximum element size of 0.2 mm, which results in 387,436 domain elements and 1200 boundary elements. Implicit backward difference formula (BDF) is chosen as the time stepping method used by the solver, with order of accuracy equal to 2. Time steps taken by solver are set to be manual, and equal to 0.1 ms. Computations take about three days to complete, using a mini workstation with a 3.30 GHz quad-core Intel® Xeon® processor, 32 GB of 2133 MHz RAM, and sufficient amount of solid state storage space. The solver uses up to 30 GB of physical memory and up to 46 GB of virtual memory.

5.1 Spatio-temporal pattern of gamma oscillations

The computation results are shown in Fig. 9, in which spatial propagation of the emerged gamma oscillations are shown at every 100 ms. Measurements of v_E at the center of regions A and B are also shown in the upper panel of Figs. 10 and 11. As predicted by the results of Section 3, modulation of F_I induces gamma oscillations in both regions, which gradually emerge and become prominent

Fig. 9 Emergence and spatial propagation of gamma oscillations in the solutions of the model (1). Each frame illustrates the spatial profile of v_E over Ω at the time t shown on the top of the frame. The reference of electric potential for v_E is the mean resting soma membrane potential $v_{E_{rest}} = -72.293$ mV. Insets in the bottom of the frames show the modulation state of parameters, with F_I shown on the left and F_E shown on the right. The color bar only indicates the value of v_E and does not correspond to the value of parameters shown in the insets. Transient oscillations on the lower left corner of the frames take place in region A. Sustained oscillations on the upper right corner of the frames take place in region B, where the excitatory modulation is not applied
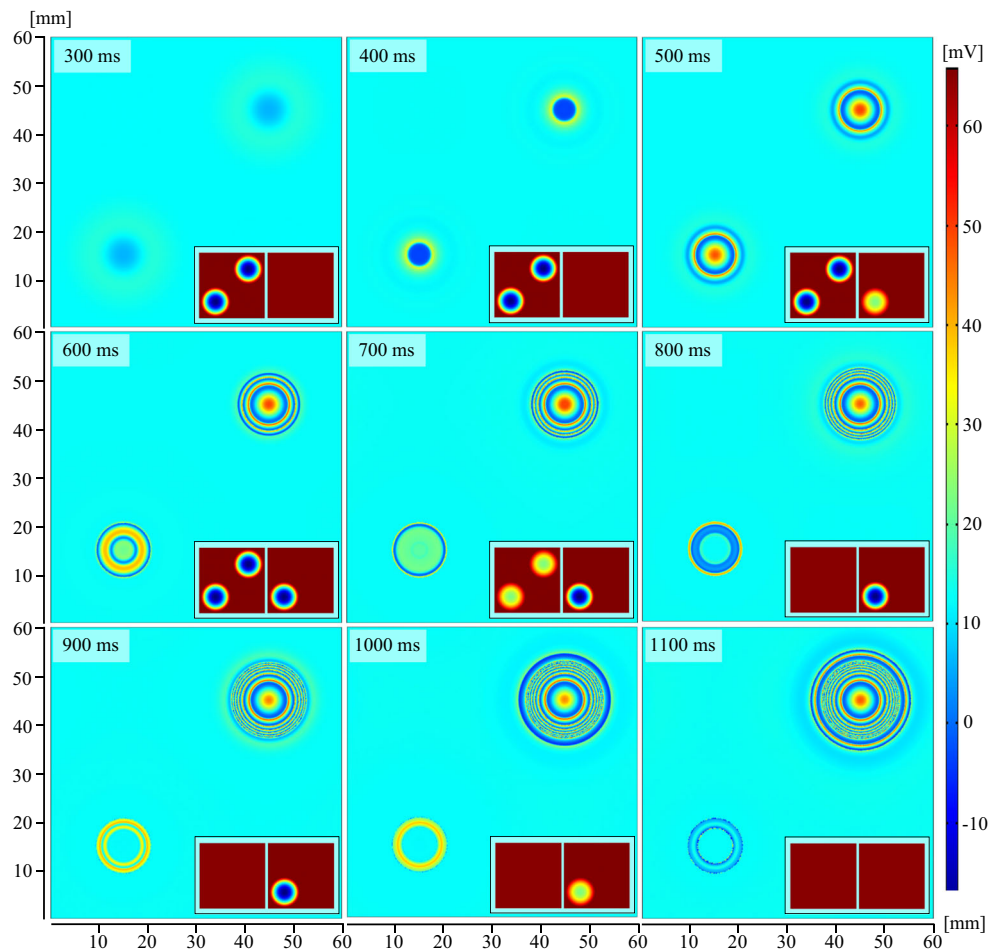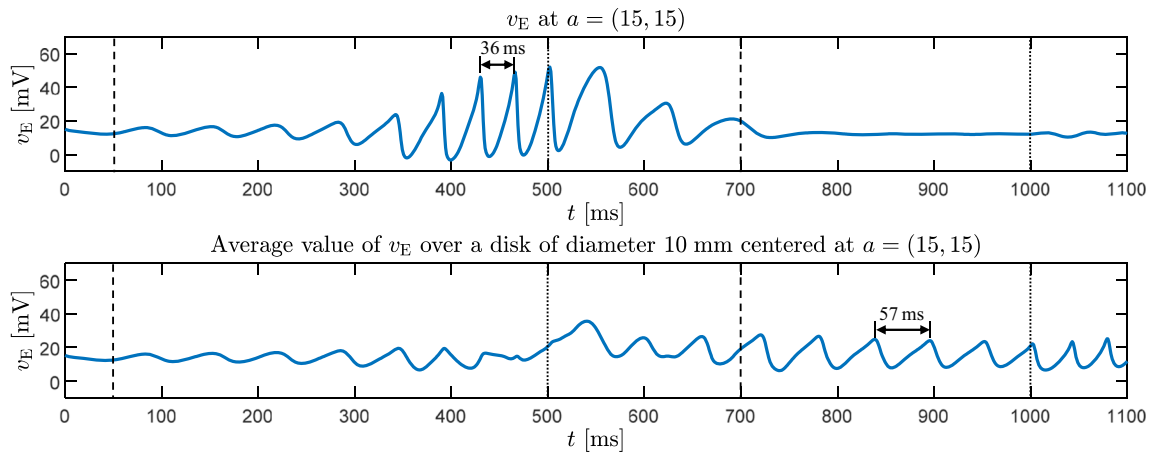
Fig. 10 Measurements of v_E in region A. Dashed lines indicate the times of transitions in F_I, and dotted lines indicate the times of transitions in F_E. The reference of electric potential for v_E is the mean resting soma membrane potential $v_{E_{rest}} = -72.293$ mV. Upper panel: point-measurements at the center of the region. Lower panel: average measurements over a disk of diameter 10 mm co-centered with the region

approximately at $t = 400$ ms. This gradual emergence of gamma oscillations, predicted by the results of Section 3 as the time required by the orbits to converge to the stable limit cycle, is usually observed during experimental studies (Ray and Maunsell 2015). Moreover, as discussed in Section 4, the emerged oscillations in region B do not vanish after F_I returns to its nominal value at $t_{I_2} = 700$ ms. However, as predicted by the mechanism described in Section 4, gamma oscillations in region A gradually vanish after the level of excitation is substantially reduced by decreasing F_E at $t_{E_1} = 500$ ms. As a result, transient gamma oscillations are observed in the measurements of region A for about three cycles and the initial resting-state is approximately restored at the end of the simulation.

Consistent with the spatial locality property of gamma oscillations stated in Section 1, the gamma oscillations appear locally within the regions where modulatory actions are applied and do not propagate to other regions of the neocortex. This is not an obvious observation, since the cortical activity inside the regions of gain modulation is also transmitted to other regions through the corticocortical communications modeled by the telegraph equations in (1). Although a rigorous mathematical proof of the existence of this localized behavior can be very involved, the intuition coming from the analysis of equilibrium sets of the model (Shirani et al. 2017, sect. 7.2) implies that the coupling between the telegraph equations and the rest of the equations of the model is not very strong. As a result, the activity propagating from the regions of gain modulation to the rest of the neocortex is not sufficiently strong to induce phase transitions in cortical networks of other regions, and hence it cannot effectively engage them in gamma oscillations.
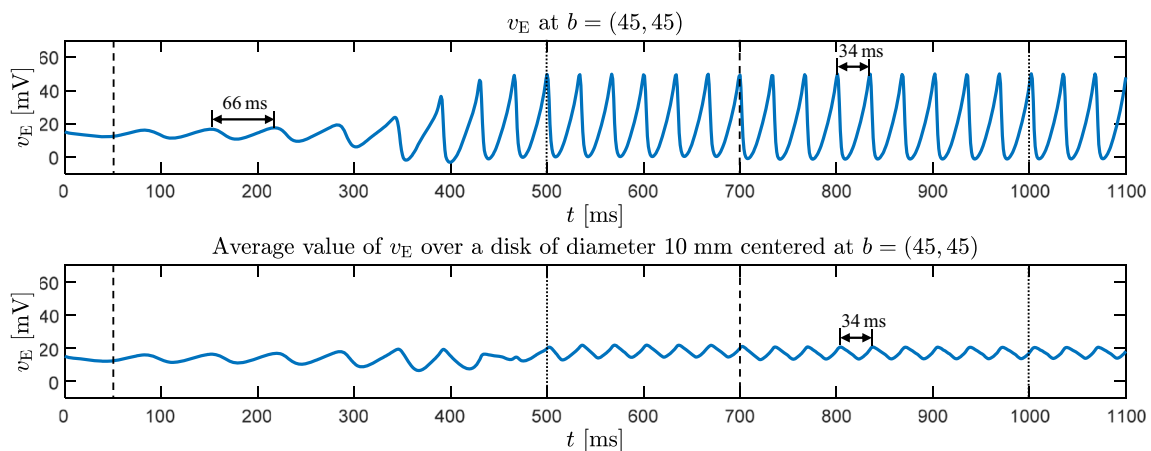

Fig. 11 Measurements of v_E in region B. The same description as given in Fig. 10 holds for dashed and dotted lines, as well as measurements of upper and lower panels

This intuition also predicts that the model can present a rich variety of localized oscillatory or non-oscillatory behavior.

Note that, a ring of oscillations in region A is still visible in Fig. 9 up to the end of the simulation. However, it can be seen in the lower panel of Fig. 10 that these oscillations are in beta band. Although the analysis of the ODE system in Section 4 is not sufficient to predict the full spatio-temporal behavior of the solutions of (1), it can provide meaningful explanation for the existence of this ring of beta oscillations. Since $\phi(x)$ decreases radially and smoothly as x approaches the boundary of the disk, the modulatory action on F_E is not as effectively applied at peripheral regions of the disk as it is applied at the central regions. Therefore, the curves of limit cycles and their frequency shown in Figs. 6a and 7a for low values of F_E imply that the dynamics of the system on the persistent ring of oscillations in region A may still be trapped on stable cycles of beta frequency and lower v_E-amplitude. Alternatively, the slowly decreasing amplitude of these beta oscillations can imply that the stable oscillations are indeed terminated in this ring-shaped region as well, but the resulting damped oscillations simply require more time to vanish, possibly due to weak damping in the dynamics of the system for the specific values that F_E takes over this region. Therefore, it is expected that these oscillations will also fade away if an stronger modulation of F_E to a lower value $\tilde{F}_E$ is applied, $\phi(x)$ is reshaped to present a sharper transition from 1 to 0, and the simulation time horizon is extended. However, these modifications are not carried out for the results presented here, to avoid excessive computational cost and to additionally illustrate part of the rich spatio-temporal behavior of the model predicted by the analytical results established by Shirani et al. (2017).

5.2 Effect of electrode size and electrode location on measurements of gamma oscillations

As shown in the upper panel of Figs. 10 and 11, the gamma oscillations measured at the center of regions A and B have relatively high amplitude. This may sound reasonable since, as stated in Section 1, gamma oscillations usually present engagement of cortical networks in cognitive activity and hence higher levels of neuronal excitation. However, compared with the high-amplitude oscillations of low frequency that appear over a large region of neocortex during deep sleep, electrocortical measurements of gamma oscillations usually have low amplitude (Ray and Maunsell 2015; Buzsáki and Wang 2012; Jia and Kohn 2011; Ni et al. 2016). A possible explanation for this perhaps unexpected observation can be provided by inspecting the propagation pattern of the oscillations in Fig. 9 and including the effect of electrode size on measurements. Note that the signals shown in the upper panel of Figs. 10 and 11 are point-measurements at the center of regions A and B. However, EEG electrodes are, typically, disks of $5 - 10$ mm in diameter. Therefore, they collectively measure the activity of many adjacent cortical networks distributed over the measurement range of the electrode. To approximately incorporate the effect of this collective measurement, the average value of v_E over disks of diameter 10 mm co-centered with regions A and B are shown in the lower panel of Figs. 10 and 11. It is observed that, while the frequency of gamma oscillations remains unchanged, their amplitude is drastically reduced in the average measurements. This is due to the propagation pattern of the oscillations within the range of electrodes. The spatial pattern of oscillations in region B in Fig. 9 shows that the gamma oscillations
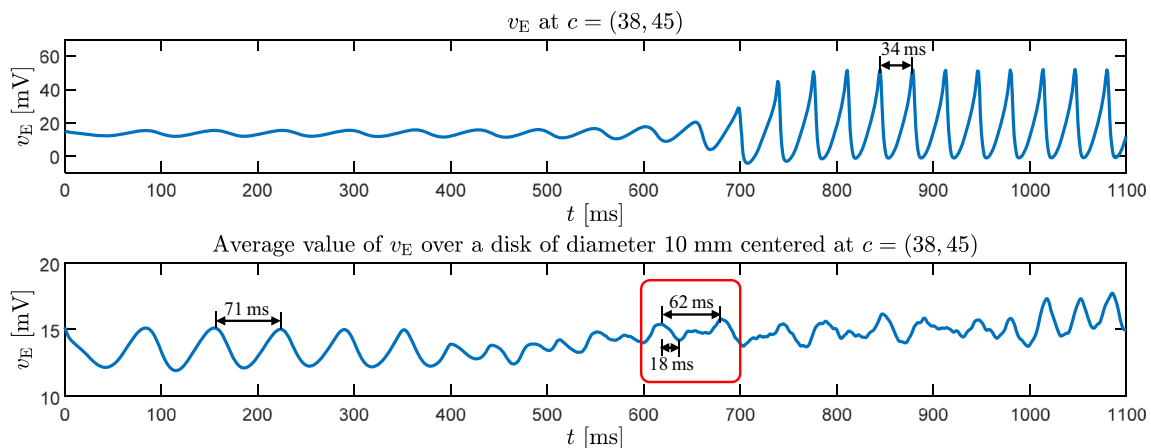

Fig. 12 Measurements of v_E associated with an electrode which is dislocated from the center of region B. The reference of electric potential for v_E is the mean resting soma membrane potential $v_{E_{rest}} = -72.293$ mV. Note the different scales used for the vertical axis of the panels. Upper panel: point-measurements at $c = (38, 45)$. Lower panel: average measurements over a disk of diameter 10 mm centered at $c = (38, 45)$.

emerging at the center of the region propagate radially to peripheral areas forming spatial waves of very short length. An electrode of diameter 10 mm collectively measures the electrical activity over a number of these waves of oscillations. Consequently, the effect of oscillatory activity of a local network on overall measurement of the electrode can effectively be canceled by the anti-phase oscillations of an adjacent network, so that the amplitude of the overall measurement is substantially reduced.

The spatial locality of gamma oscillations makes the location of electrodes important. To observe this, the 10 mm electrode centered at region B is relocated from the center to the point $c = (38, 45)$, so that it overlaps both with the regions where gamma oscillations emerge and with the regions where oscillations remain in beta band. Point-measurements at c and average measurements of the electrode are shown in Fig. 12. Comparing the average measurements before and after relocating the electrode shows that a relatively wide spectrum of low power oscillations, even in high gamma band, are introduced into the measurements as a result of dislocation of the electrode from the center of propagating gamma oscillations. In particular, comparing the two panels of Fig. 12 with each other identifies a time interval over which the waves of gamma oscillations have not reached the center of the electrode but are sufficiently overlapped by the electrode so that they effectively introduce ripples of gamma frequency into the measurements. This interval is marked by a red square in Fig. 12. The measurements over this interval present a ripple of gamma frequency superimposed on a cycle of beta oscillations. This can be misinterpreted as an implication of correlation between beta and gamma oscillations, while it is in fact nothing but the result of collective measurements from different networks, some of which oscillating at beta frequency and others at gamma frequency.

6 Discussion and conclusion

Using a spatio-temporal model of electrocortical activity, the results presented above explain plausible mechanisms for robust induction of transient gamma oscillations by coordinated modulation of the responsiveness of neuronal populations. The results confirm the locality of gamma oscillations and demonstrate possible patterns of spatial propagation of these oscillations across local regions of the neocortex. Moreover, they predict potential impacts of the size and location of electrocortical measurement electrodes on the amplitude, temporal pattern, and frequency spectrum of the oscillation measurements.

Specifically, the results of Sections 3 and 4 show that sufficient decrease in sensitivity (gain) and excitability (response threshold) of inhibitory populations, as well as

sufficient increase in their saliency, can robustly induce gamma oscillations within the regions where the modulatory actions are applied. Similarly, gamma oscillations can also be induced by effectively increasing the sensitivity and excitability of excitatory populations as well as decreasing their saliency. In all these cases, the gamma oscillations emerge as stable limit cycles when the dynamics of the cortical networks presented by the model undergoes a Hopf bifurcation. Regardless of the type of modulations used to induce the gamma oscillation, either excitatory or inhibitory, a subsequent modulation of excitatory population for reduction in the level of excitation is necessary and sufficient for termination of the emerged oscillations and transition to low beta oscillations. This is consistent with the observations available in the literature that identify the excitatory activity of pyramidal cells as the driving force of the oscillations (Buzsáki and Wang 2012; Kopell et al. 2000; Cardin et al. 2009).

The results of this paper further emphasize the importance of developing detailed mechanistic models to unveil the actual sequence of causal relations leading to the emergence and termination of gamma oscillations. Electrophysiological, behavioral, and optogenetic studies of cortical networks have shown that visually and optogenetically induced gamma oscillations modulate neuronal gain (Ni et al. 2016; Cardin et al. 2009). In the seemingly opposite causal direction, however, sensory-driven barrages of synaptic inputs are shown to modulate neuronal gain (Cardin et al. 2008; Haider and McCormick 2009), which consequently can induce gamma oscillations according to the analysis of Section 3. Moreover, termination of the emerged gamma oscillations and their transition to beta oscillations—most likely through substantial reduction in the level of network excitation—is predicted by the results of Section 4 to require specific modulation of excitatory populations. The mechanism of this subsequent modulation and its direct cellular or network causes require further investigation. In particular, when gamma oscillations are initially induced by modulation of inhibitory populations, the analysis of Section 4 shows that this subsequent modulation of excitatory populations is in the direction of restoring the balance of excitation and inhibition in the network. Therefore, it can be postulated that the modulatory actions that result in transition to beta oscillations are the reaction of the cortical network to the imbalance created by the initial, possibly stimulus-driven, modulation. As a result, long-lasting gamma oscillations in the absence of effective neuromodulators or streams of synaptic activity may be assumed as the failure of the network in re-establishing its balance, possibly due to a neuronal disorder.

Propagating waves of gamma oscillations, as demonstrated in Section 5, can be of very short length compared with the diameter of a typical EEG electrode. As a result,

the collective measurements of these waves of activity by an electrode shows significantly lower amplitude oscillations compared with point-measurements. Low amplitude of gamma oscillations has led to interpretations that gamma oscillations are nothing but fluctuations at a resonance frequency of cortical networks (Jia and Kohn 2011). The results presented here, however, do not support such interpretations. The gamma oscillations in the solutions of the model emerge as a result of a phase transition in the dynamics of local cortical networks, which is robustly evoked by systematic modulation of neuronal responsiveness.

Due to the locality and propagation pattern of gamma oscillations, the location of measurement electrodes relative to the regions of gamma activity can significantly affect the temporal pattern of measurements so that ripples in broad range of frequency are introduced—even for the simple flat geometry considered for the neocortex in the computational results of Section 5. In particular, as shown in Section 5.2, measurements of an electrode which overlaps with both regions of beta and gamma oscillations can potentially result in misinterpretations about the network dynamics of gamma and beta rhythmic activity, possible correlations between these oscillations, and mechanisms of frequency shifts from gamma to beta in cortical oscillations (Traub et al. 1999; Kopell et al. 2000). Taking further into consideration that the neocortex has a convoluted geometry, these results recommend that the interpretations made solely based on the observation of specific temporal patterns in EEG recordings should be reconsidered, and possibly be validated by using other electrocortical measurement techniques, before being used to establish physiological facts. Moreover, the results discussed in Section 5.2 also demonstrate the limitations of commonly used reduced-network models to fully describe the patterns of rhythmic activity in EEG recordings. In fact, not only cannot such systems of ordinary differential equations explain spatial propagation of oscillatory waves, but also they cannot completely predict the temporal patterns of electrode measurements. Besides measurement noise and other unknown sources of perturbations, the amplitude and pattern of these temporal measurements can be highly affected by the activity of nearby networks and complicated geometry of the neocortex. Such impacts are more significant on measurements of fast oscillations which arise locally and develop waves of very short length.

The numerical analysis of Sections 3 and 4 are based on a single set of biophysically plausible parameter values given in Table 2. An automated search performed by Bojak and Liley (2005) using a stability and spectral analysis of the linearized version of the model has resulted in 73,454 sets of plausible parameter values. However, further bifurcation analysis performed by Frascoli et al. (2011) on a 405 randomly selected subset of these 73,454 parameter sets has identified only two different families of topological

structures in the dynamics of the model resulting from these different parameter sets. Moreover, these two families of dynamic structures are shown to be transformable from one family into the other by varying excitatory subcortical inputs. The bifurcation analysis presented here in Sections 3 and 4 involves numerous manual adjustments of continuation parameters in MatCont; see the Appendix. Therefore, an automated search within a large subset of the available 73,454 parameter sets, aimed to identify the parameter values that result in similar qualitative behaviors as shown in Sections 3 and 4, requires specifically developed numerical analysis tools and can be a topic of future research. Instead, the bifurcation analysis of Sections 3 and 4 is repeated here for several other parameter sets, which are generated by randomly perturbing the values given in Table 2 by a magnitude of 10 to 100 percent. The results obtained for a sample of such sets are given in the Appendix. Specifically, it is observed that the analysis is very robust against changes in the membrane time constant of the neurons, whereas it is relatively more sensitive to changes in postsynaptic potential rate constants.

Finally, a note on the numerical computation of the solutions of the model (1) can be of interest for future studies using this model. As the computations of Section 5 proceed in time, the propagating waves in some components of the solutions become exceedingly fine. Although the discretization mesh used for the computation is extremely fine, it still cannot result in completely accurate solutions of these waves. As a result, some irregularities can be observed in the shape of waves in Fig. 9 when the simulation approaches its end. Therefore, more accurate solutions over a longer time horizon requires significantly finer mesh which substantially increases the computational cost of the simulation. These irregularities are observed in the solution components $v = (v_E, v_I)$ and $i = (i_{EE}, i_{EI}, i_{IE}, i_{II})$, whereas the solution component $w = (w_{EE}, w_{EI})$ does not develop waves of very short length and evolves smoothly in time and space. These observations are confirmed by the analytical results developed by Shirani et al. (2017), which particularly predict that v and i components of solutions can develop drastic asymptotic discontinuities in space, regardless of the smoothness of initial values and subcortical forcing terms.

Compliance with Ethical Standards

Appendix: Bifurcation analysis results for a different set of parameter values

To show the robustness of the results of Sections 3 and 4 against changes in parameter values, the bifurcation analysis

Table 3 A set of parameter values generated by perturbations of magnitude 10 to 100 percent in the values given in Table 2. This set of values is used as nominal parameter values for the computational results presented in the Appendix

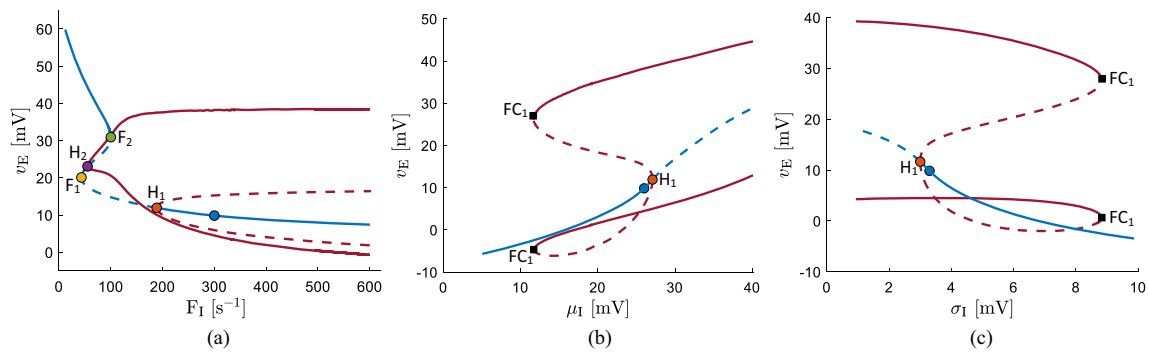| Parameter	τ_E	τ_I	V_{EE}	V_{EI}	V_{IE}	V_{II}	γ_{EE}	γ_{EI}	γ_{IE}	γ_{II}	Υ_{EE}
Value	65×10^{-3}	65×10^{-3}	67	89	-9.3	-8.5	110	850	315	125	0.25
Parameter	Υ_{EI}	Υ_{IE}	Υ_{II}	N_{EE}	N_{EI}	N_{IE}	N_{II}	ν	$\Lambda_{EE}, \Lambda_{EI}$	M_{EE}	M_{EI}
Value	1.25	1.00	0.25	3570	4140	490	345	140	0.5	3550	2510
Parameter	F_E	F_I	μ_E	μ_I	σ_E	σ_I	$\bar{g}_{EE}$	$\bar{g}_{EI}$	$\bar{g}_{IE}$	$\bar{g}_{II}$	
Value	93	300	26	26	4.2	3.3	3150	5670	0	0	

Fig. 13 Codimension-one bifurcation diagrams of the ODE system described in Section 3 for the nominal parameter values given in Table 3. The same description as given in Fig. 2 holds for the curves of equilibria and limit cycles, as well as the detected bifurcation points
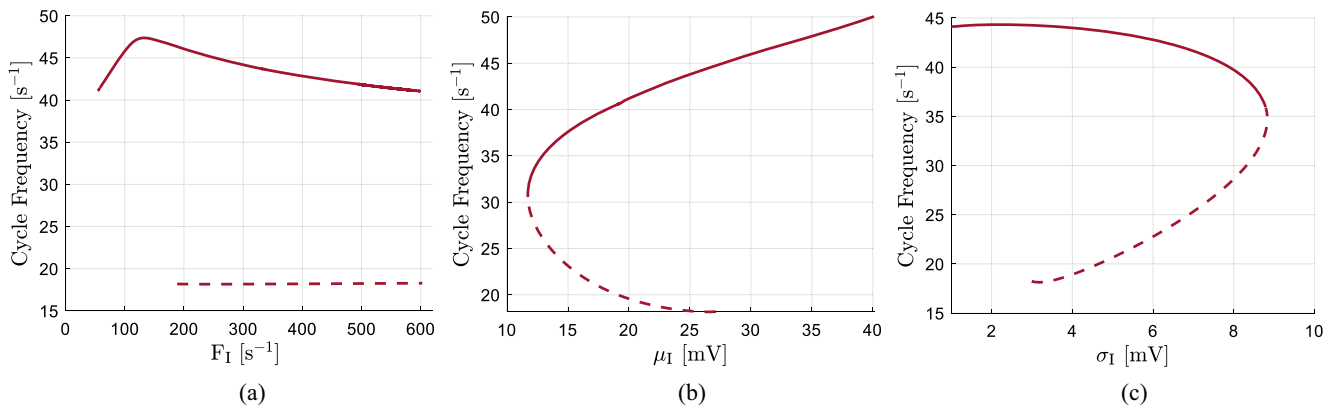

Fig. 14 Frequency of the limit cycles in the bifurcation diagrams shown in Fig. 13
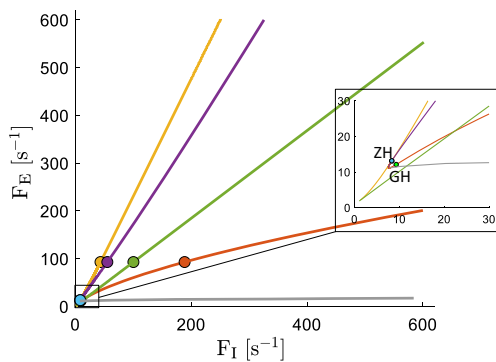
Fig. 15 Two-parameter continuation of the bifurcation points shown in Fig. 13a. The starting bifurcation points are indicated by dots with the same colors as they appear in Fig. 13a. The curve shown in gray is the result of the continuation of a fold bifurcation of limit cycles that is not made visible in Fig. 13a. The detected codimension-two zero-Hopf bifurcation point is indicated by ZH. The detected codimension-two generalized Hopf bifurcation point is indicated by GH

of these sections is repeated in this appendix for a different set of parameter values as given in Table 3. These parameter values are generated by randomly perturbing the values used in Sections 3 and 4 by a magnitude of 10 to 100 percent. The codimension-one bifurcation diagrams and the frequency of the limit cycles are shown in Figs. 13 and 14. These diagrams resemble the diagrams shown in Figs. 2 and 3, respectively, and equivalently imply the emergence of gamma oscillations as a result of a Hopf bifurcation. The result of two-parameter continuation of the bifurcation points detected in Fig. 13a for neuronal sensitivity modulation is shown in Fig. 15. The bifurcation diagrams for the nominal value of F_E given in Table 3, as well as the diagram for a modulated lower value of

$F_E = 13$ [s^{-1}] are shown in Fig. 16, which illustrates the coordinated transition from gamma oscillations to the initial resting state. The results are highly comparable to the results obtained in Section 4. Similarly, two-parameter analysis of excitability (μ_E and μ_I) and saliency (σ_E and σ_I) modulations leads to results very close to those obtained in Section 4, and hence are not included here.

A note on using MatCont for the numerical bifurcation analysis of this paper can be of interest for future works on this model. The MatCont versions 6.6 and 7.1 were used to perform the computations. To achieve convergence and obtain the full extent of the curves presented in the bifurcation diagrams, the continuation parameters are usually needed to be re-adjusted manually for each diagram. These re-adjustments are especially needed when continuing the curves of limit cycles and their fold bifurcations. The convergence error typically observed is 'current step size too small'. The direction of the continuation of limit cycles may occasionally be reversed during the continuation, especially near the fold bifurcations. No general rule was observed for adjusting the continuation parameters so that these problems are resolved. However, setting the number of mesh points equal to 6 and the number of collocation points equal to 5 usually results in smoother continuation of the limit cycles. Adjustment of the initial amplitude can affect the convergence of the continuations. A value between 0.1 to 5 was typically chosen for this parameter. Finally, adjustment of the maximum step size MaxStepsize option for continuation of the limit cycles is frequently needed to resolve convergence errors or to avoid reversals in the direction of continuation. Values as large as 50000 or larger for MaxStepsize are needed in some cases.

References

Bojak, I., & Liley, D.T.J. (2005). Modeling the effects of anesthesia on the electroencephalogram. *Physical Review E*, *71*, 041902. https://doi.org/10.1103/PhysRevE.71.041902.

Bojak, I., & Liley, D.T.J. (2007). Self-organized 40 Hz synchronization in a physiological theory of EEG. *Neurocomputing*, *70*(10–12), 2085–2090. https://doi.org/10.1016/j.neucom.2006.10.087.

Bojak, I., Liley, D.T.J., Cadusch, P., Cheng, K. (2004). Electrorhythmogenesis and anaesthesia in a physiological mean field theory. *Neurocomputing*, *58–60*, 1197–1202. https://doi.org/10.1016/j.neucom.2004.01.185.

Bojak, I., Day, H.C., Liley, D.T.J. (2013). Ketamine, propofol and the EEG: A neural field analysis of HCN1-mediated interactions. Frontiers in Computational Neuroscience 7(22). https://doi.org/10.3389/fncom.2013.00022.

Bojak, I., Stoyanov, Z.V., Liley, D. (2015). Emergence of spatially heterogeneous burst suppression in a neural field model of electrocortical activity. Frontiers in Computational Neuroscience 9(18). https://doi.org/10.3389/fnsys.2015.00018.
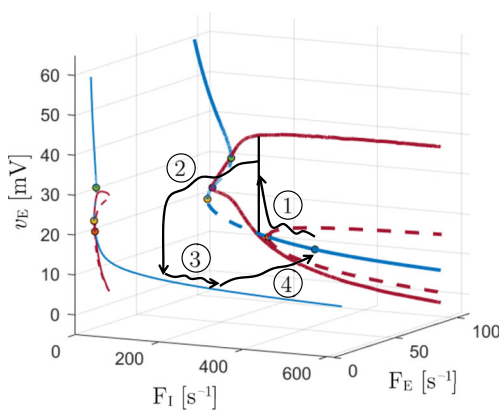
Fig. 16 Mechanism of transient emergence of gamma oscillations through coordinated modulation of inhibitory and excitatory neuronal sensitivity. The diagrams are obtained using the parameter values described in the Appendix. The description of the modulatory actions and phase transitions in Steps 1 to 4 follows the same description as given in Fig. 8

Buzsáki, G., & Wang, X.J. (2012). Mechanisms of gamma oscillations. *Annual Review of Neuroscience*, *35*(1), 203–225. https://doi.org/10.1146/annurev-neuro-062111-150444.

Buzsáki, G., & Watson, B.O. (2012). Brain rhythms and neural syntax: implications for efficient coding of cognitive content and neuropsychiatric disease. *Dialogues in Clinical Neuroscience*, *14*(4), 345–367.

Cardin, J.A., Palmer, L.A., Contreras, D. (2008). Cellular mechanisms underlying stimulus-dependent gain modulation in primary visual cortex neurons in vivo. *Neuron*, *59*(1), 150–160. https://doi.org/10.1016/j.neuron.2008.05.002.

Cardin, J.A., Carlén, M., Meletis, K., Knoblich, U., Zhang, F., Deisseroth, K., Tsai, L., Moore, C.I. (2009). Driving fast-spiking cells induces gamma rhythm and controls sensory responses. *Nature*, *459*, 663–667. https://doi.org/10.1038/nature08002.

Dafilis, M.P., Liley, D.T.J., Cadusch, P.J. (2001). Robust chaos in a model of the electroencephalogram: Implications for brain dynamics. *Chaos*, *11*(3), 474–478. https://doi.org/10.1063/1.1394193.

Dafilis, M.P., Frascoli, F., Cadusch, P.J., Liley, D.T.J. (2013). Four dimensional chaos and intermittency in a mesoscopic model of the electroencephalogram. *Chaos*, *23*(2), 023111. https://doi.org/10.1063/1.4804176.

Dafilis, M.P., Frascoli, F., Cadusch, P.J., Liley, D.T.J. (2015). Extensive four-dimensional chaos in a mesoscopic model of the electroencephalogram. The Journal of Mathematical Neuroscience 5(1). https://doi.org/10.1186/s13408-015-0028-3.

Dehghani, N., Peyrache, A., Telenczuk, B., Quyen, M.L.V., Halgren, E., Cash, S.S., Hatsopoulos, N.G., Destexhe, A. (2016). Dynamic balance of excitation and inhibition in human and monkey neocortex. *Scientific Reports*, *6*, 23176. https://doi.org/10.1038/srep23176.

Dhooge, A., Govaerts, W., Kuznetsov, Y.A., Meijer, H.G.E., Sautois, B. (2008). New features of the software MatCont for bifurcation analysis of dynamical systems. *Mathematical and Computer Modelling of Dynamical Systems*, *14*(2), 147–175. https://doi.org/10.1080/13873950701742754.

Disney, A.A., Aoki, C., Hawken, M.J. (2007). Gain modulation by nicotine in macaque v1. *Neuron*, *56*(4), 701–713. https://doi.org/10.1016/j.neuron.2007.09.034.

van Ede, F., Quinn, A.J., Woolrich, M.W., Nobre, A.C. (2018). Neural oscillations: Sustained rhythms or transient burst-events? *Trends in Neurosciences*, *41*(7), 415–417. https://doi.org/10.1016/j.tins.2018.04.004.

Fino, E., & Yuste, R. (2011). Dense inhibitory connectivity in neocortex. *Neuron*, *69*(6), 1188–1203. https://doi.org/10.1016/j.neuron.2011.02.025.

Foster, B.L., Bojak, I., Liley, D.T.J. (2008). Population based models of cortical drug response: insights from anaesthesia. *Cognitive Neurodynamics*, *2*(4), 283–296. https://doi.org/10.1007/s11571-008-9063-z.

Frascoli, F., Dafilis, M.P., van Veen, L., Bojak, I., Liley, D.T.J. (2008). Dynamical complexity in a mean-field model of human EEG. *Proceedings of SPIE*, *7270*, 72700V–72700V–10. https://doi.org/10.1117/12.813966.

Frascoli, F., van Veen, L., Bojak, I., Liley, D.T.J. (2011). Metabifurcation analysis of a mean field model of the cortex. *Physica D: Nonlinear Phenomena*, *240*(11), 949–962. https://doi.org/10.1016/j.physd.2011.02.002.

Green, K.R., & van Veen, L. (2014). Open-source tools for dynamical analysis of Liley's mean-field cortex model. *Journal of Computational Science*, *5*(3), 507–516. https://doi.org/10.1016/j.jocs.2013.06.001.

Haider, B., & McCormick, D.A. (2009). Rapid neocortical dynamics: Cellular and network mechanisms. *Neuron*, *62*(2), 171–189. https://doi.org/10.1016/j.neuron.2009.04.008.

Herrero, J.L., Gieselmann, M.A., Thiele, A. (2017). Muscarinic and nicotinic contribution to contrast sensitivity of macaque area V1 neurons. *Frontiers in Neural Circuits*, *11*, 106. https://doi.org/10.3389/fncir.2017.00106.

Jia, X., & Kohn, A. (2011). Gamma rhythms in the brain. *PLOS Biology*, *9*(4), e1001045. https://doi.org/10.1371/journal.pbio.1001045.

Jones, S.R. (2016). When brain rhythms aren't 'rhythmic': implication for their mechanisms and meaning. *Current Opinion in Neurobiology*, *40*, 72–80. https://doi.org/10.1016/j.conb.2016.06.010, systems neuroscience.

Knoblich, U., Siegle, J., Pritchett, D., Moore, C.I. (2010). What do we gain from gamma? Local dynamic gain modulation drives enhanced efficacy and efficiency of signal transmission. *Frontiers in Human Neuroscience*, *4*, 185. https://doi.org/10.3389/fnhum.2010.00185.

Kopell, N., Ermentrout, G.B., Whittington, M.A., Traub, R.D. (2000). Gamma rhythms and beta rhythms have different synchronization properties. *Proceedings of the National Academy of Sciences*, *97*(4), 1867–1872. https://doi.org/10.1073/pnas.97.4.1867.

Kramer, M.A., Kirsch, H.E., Szeri, A.J. (2005). Pathological pattern formation and cortical propagation of epileptic seizures. *Journal of the Royal Society Interface*, *2*, 113–127. https://doi.org/10.1098/rsif.2005.0028.

Kramer, M.A., Szeri, A.J., Sleigh, J.W., Kirsch, H.E. (2006). Mechanisms of seizure propagation in a cortical model. *Journal of Computational Neuroscience*, *22*(1), 63–80. https://doi.org/10.1007/s10827-006-9508-5.

Kramer, M.A., Truccolo, W., Eden, U.T., Lepage, K.Q., Hochberg, L.R., Eskandar, E.N., Madsen, J.R., Lee, J.W., Maheshwari, A., Halgren, E., Chu, C.J., Cash, S.S. (2012). Human seizures self-terminate across spatial scales via a critical transition. *Proceedings of the National Academy of Sciences*, *109*(51), 21116–21121. https://doi.org/10.1073/pnas.1210047110.

Lee, C.K., & Huguenard, J.R. (2011). Martinotti cells: Community organizers. *Neuron*, *69*(6), 1042–1045. https://doi.org/10.1016/j.neuron.2011.03.003.

Lee, S., & Jones, S.R. (2013). Distinguishing mechanisms of gamma frequency oscillations in human current source signals using a computational model of a laminar neocortical network. *Frontiers in Human Neuroscience*, *7*, 869. https://doi.org/10.3389/fnhum.2013.00869.

Liley, D.T.J., & Bojak, I. (2005). Understanding the transition to seizure by modeling the epileptiform activity of general anesthetic agents. *Journal of Clinical Neurophysiology*, *22*(5), 300–313. https://doi.org/10.1097/01.wnp.0000184049.57793.0b.

Liley, D.T.J., & Walsh, M. (2013). The mesoscopic modelling of burst suppression during anaesthesia. Frontiers in Computational Neuroscience 7(46). https://doi.org/10.3389/fncom.2013.00046.

Liley, D.T.J., Cadusch, P.J., Dafilis, M.P. (2002). A spatially continuous mean field theory of electrocortical dynamics. *Network: Computation in Neural Systems*, *13*, 67–113. https://doi.org/10.1080/net.13.1.67.113.

Lopour, B.A., Tasoglu, S., Kirsch, H.E., Sleigh, J.W., Szeri, A.J. (2011). A continuous mapping of sleep states through association of EEG with a mesoscale cortical model. *Journal of Computational Neuroscience*, *30*(2), 471–487. https://doi.org/10.1007/s10827-010-0272-1.

Martinet, L.E., Fiddyment, G., Madsen, J.R., Eskandar, E.N., Truccolo, W., Eden, U.T., Cash, S.S., Kramer, M.A. (2017). Human seizures couple across spatial scales through travelling wave dynamics. *Nature Communications*, *8*, 14896. https://doi.org/10.1038/ncomms14896.

McCormick, D.A. (1992). Neurotransmitter actions in the thalamus and cerebral cortex and their role in neuromodulation of

thalamocortical activity. *Progress in Neurobiology*, *39*(4), 337–388. https://doi.org/10.1016/0301-0082(92)90012-4.

McCormick, D.A., Wang, Z., Huguenard, J. (1993). Neurotransmitter control of neocortical neuronal activity and excitability. *Cerebral Cortex*, *3*(5), 387–398. https://doi.org/10.1093/cercor/3.5.387.

Ni, J., Wunderle, T., Lewis, C.M., Desimone, R., Diester, I., Fries, P. (2016). Gamma-rhythmic gain modulation. *Neuron*, *92*(1), 240–251. https://doi.org/10.1016/j.neuron.2016.09.003.

Ray, S., & Maunsell, J.H.R. (2015). Do gamma oscillations play a role in cerebral cortex? *Trends in Cognitive Sciences*, *19*(2), 78–85. https://doi.org/10.1016/j.tics.2014.12.002.

Shirani, F., Haddad, W.M., de la Llave, R. (2017). On the global dynamics of an electroencephalographic mean field model of the neocortex. *SIAM Journal on Applied Dynamical Systems*, *16*(4), 1969–2029. https://doi.org/10.1137/16M1098577.

Steyn-Ross, D.A., Steyn-Ross, M.L., Sleigh, J.W., Wilson, M.T., Gillies, I.P., Wright, J.J. (2005). The sleep cycle modelled as a cortical phase transition. *Journal of Biological Physics*, *31*(3), 547–569. https://doi.org/10.1007/s10867-005-1285-2.

Steyn-Ross, M.L., Steyn-Ross, D.A., Sleigh, J.W. (2004). Modelling general anaesthesia as a first-order phase transition in the cortex. *Progress in Biophysics and Molecular Biology*, *85*(2–3), 369–385. https://doi.org/10.1016/j.pbiomolbio.2004.02.001.

Thurley, K., Senn, W., Lüscher, H. R. (2008). Dopamine increases the gain of the input-output response of rat prefrontal pyramidal neurons. *Journal of Neurophysiology*, *99*(6), 2985–2997. https://doi.org/10.1152/jn.01098.2007.

Traub, R.D., Whittington, A.M., Buhl, E.H., Jefferys, J.G.R., Faulkner, H.J. (1999). On the mechanism of the $\gamma \rightarrow \beta$ frequency shift in neuronal oscillations induced in rat hippocampal slices by tetanic stimulation. *Journal of Neuroscience*, *19*(3), 1088–1105. https://doi.org/10.1523/JNEUROSCI.19-03-01088.1999.

van Veen, L., & Green, K.R. (2014). Periodic solutions to a mean-field model for electrocortical activity. *The European Physical Journal Special Topics*, *223*(13), 2979–2988. https://doi.org/10.1140/epjst/e2014-02311-y.

van Veen, L., & Liley, D.T.J. (2006). Chaos via Shilnikov's saddle-node bifurcation in a theory of the electroencephalogram. *Physical Review Letters*, *97*, 208101. https://doi.org/10.1103/PhysRevLett.97.208101.

Whittington, M.A., Traub, R.D., Kopell, N., Ermentrout, B., Buhl, E.H. (2000). Inhibition-based rhythms: experimental and mathematical observations on network dynamics. *International Journal of Psychophysiology*, *38*(3), 315–336. https://doi.org/10.1016/S0167-8760(00)00173-2.

Wilson, M.T., Marcus, T., Sleigh, J.W., Steyn-Ross, D.A., Steyn-Ross, M.L. (2006a). General anesthetic-induced seizures can be explained by a mean-field model of cortical dynamics. *Anesthesiology*, *104*(3), 588–593.

Wilson, M.T., Steyn-Ross, D.A., Sleigh, J.W., Steyn-Ross, M.L., Wilcocks, L.C., Gillies, I.P. (2006b). The K-complex and slow oscillation in terms of a mean-field cortical model. *Journal of Computational Neuroscience*, *21*(3), 243–257. https://doi.org/10.1007/s10827-006-7948-6.